Titre: Title:	Viscosity of fluoride glass fibers for fused components fabrication
Auteurs: Authors:	Edith Ducharme, Stéphane Virally, Rodrigo Itzamna Becerra Deana, Caroline Boudoux, & Nicolas Godbout
Date:	2022
Type:	Article de revue / Article
Référence: Citation:	Ducharme, E., Virally, S., Becerra Deana, R. I., Boudoux, C., & Godbout, N. (2022). Viscosity of fluoride glass fibers for fused components fabrication. Applied Optics, 61(17), 5031-5039. https://doi.org/10.1364/ao.455528

Titre de la revue: Journal Title:	Applied Optics (vol. 61, no. 17)
Maison d'édition: Publisher:	Optical Society of America
URL officiel: Official URL:	https://doi.org/10.1364/ao.455528
Mention légale: Legal notice:	© 2022 Optica Publishing Group under the terms of the Optica Open Access Publishing Agreement

Research Article Vol. 61, No. 17 / 10 June 2022 / Applied Optics 5031

applied optics

Viscosity of fluoride glass fibers for fused component fabrication

Édith Ducharme,[1] Stéphane Virally,[1] Rodrigo Itzamná Becerra-Deana,[1,2] Caroline Boudoux,[1,2] and Nicolas Godbout[1,2,*]

[1]Polytechnique Montréal, Department of Engineering Physics, 2500, Chemin de Polytechnique, Montréal, Québec H3T 1J4, Canada
[2]Castor Optics, Inc., 361 Boul Montpellier, Saint-Laurent, Quebec H4N 2G6, Canada
*Corresponding author: nicolas.godbout@polymtl.ca

Received 4 February 2022; revised 25 April 2022; accepted 9 May 2022; posted 10 May 2022 (Doc. ID 455528); published 2 June 2022

Fluoride glasses show great promise for mid-IR fiber-based applications. Their brittleness and low glass transition temperature have thus far been obstacles towards obtaining low-loss fused components. Here, we suggest a simple method to measure glass viscosity over a range of process temperatures of interest for fused coupler fabrication. We achieved tapers of inverse taper ratio (ITR) 0.12 in multimode fluoroindate fibers. Tapers with loss <0.1 dB at ITR 0.3 and no visible defects were fabricated with high repeatability. This work paves the way towards low-loss fused optical couplers in fluoride glass fiber.

https://doi.org/10.1364/AO.455528

1. INTRODUCTION

For several decades, fused-silica-based optical fiber components have been the gold standard for low-loss connections within optical circuits [1,2]. State-of-the-art components go well beyond single-mode (SM) and multimode (MM) fiber applications. For instance, double-clad fiber couplers (DCFCs) [3] combine properties of SM and MM couplers by using a double-clad fiber. Biomedical applications such as new contrast imaging techniques [4], endoscopy prototypes [5–8], and laser therapy [9,10] in the visible and near-infrared (IR) regions are among the many applications benefiting from novel fused optical fiber couplers. The mid-IR region, defined as the range of wavelengths between 3 and 5 μm, shows tremendous potential for multiple applications: spectroscopy [11], chemical sensing [12], and biomedical applications, such as biomarking [13] and tissue ablation [14]. However, silica becomes opaque at wavelengths exceeding ∼2 μm.

The development of mid-IR fluoride glass fibers was a game changer. It led to all-fiber sources [15,16] usable inside and outside laboratories. However, an important element is still missing: monolithic, compact, and robust systems for industrial and clinical applications in the mid-IR require low-loss fiber components with characteristics similar to their silica counterparts. Very few components have been demonstrated, even though mid-IR fibers are now commonplace. Some applications such as all-fiber optical amplifiers for the mid-IR [17] currently rely on polished fluoride fiber couplers [18]. Fused couplers have also been demonstrated [19], albeit with high excess loss. There remains an unmet need for low-loss fluoride glass optical components.

The fabrication of fused fiber couplers implies heating two fibers near their glass transition temperature, fusing them, and then tapering them to allow electromagnetic field coupling. Fiber tapers, whether used in couplers or as standalone on a single fiber, are themselves components of interest. They are used in numerous applications, including as probes for the detection of water pollutants [20] and as biomarkers [21]. As silica has been extensively studied [22], design parameters are well established for fused silica components [23,24]. In contrast, fluoride glass fibers present various challenges, as their critical mechanical properties complicate manipulations. In addition to their fragility [25], crystallization and steep viscosity variation around their glass transition temperature impose very strict control over the processing temperature [26]. In particular, viscosity is a key parameter that must be well managed during the fabrication process. Herein, we present a study of the viscosity of fluoride glass fibers near their glass transition temperature. Our method of measurement represents a paradigm change in the way viscosity is measured, as it brings the conditions of measurement close to the conditions of device fabrication: bulk viscosity measurements [27,28] are not necessarily easily related to fiber viscosities. We first develop a model of strain versus time for optical fibers submitted to a longitudinal force. The model features viscosity as the single free parameter so that fits of experimental curves directly yield viscosity values for a range of conditions, and in particular, glass temperature. This enables us to define optimal windows of process temperatures for the fabrication of fused components. As a first step towards robust and repeatable fused fluoride glass fiber couplers, we show that

using the right process temperature range allows the fabrication of low-loss fluoride fiber tapers.

Two main types of fluoride glass optical fibers exist. The first is fluorozirconate-based fibers, with one of its most common conformations being ZBLAN (ZrF_4 , BaF_2 , LaF_3 , AlF_3 , NaF). These glasses are transparent up to 4.5 μm [29]. Powerful laser sources in ZBLAN fiber are already common, making this type of glass an interesting candidate for mid-IR applications [30]. The second type is fluoroindate (InF_3). Although fluoroindate fibers are not as mature as ZBLAN fibers, their transparency up to 5.5 μm extends the usable spectral range in comparison to ZBLAN fibers [31]. In this work, we study both ZBLAN and fluoroindate fibers.

2. STRAIN AND VISCOSITY

The strain rate $\partial\epsilon/\partial t$ of a fiber under longitudinal stress depends on the applied load and viscosity of the glass. It is thus possible to infer viscosity from strain curves. We first model the theoretical strain for an arbitrary taper shape in Subsection 2.A. In Subsection 2.B, we apply the theory to a specific taper shape to find a strain function to fit our data with viscosity as the single free parameter.

A. Geometrical Model

An optical fiber under tensile force F will stretch at its smallest cross section (waist) at a strain rate of

$$\frac{\partial\epsilon}{\partial t} = \frac{F}{\eta_e S}, \tag{1}$$

where S is the time-varying waist cross section and η_e the elongational viscosity (subsequently called viscosity).

The time-varying strain is defined as

$$\epsilon = \frac{L - L_0}{L_0}, \tag{2}$$

with L_0 the initial length of the stretched section and L its time-varying length.

Differentiating Eq. (2) with respect to t, we find

$$\frac{\mathrm{d}L}{L_0} = \frac{F}{\eta_e S}\mathrm{d}t. \tag{3}$$

We link the varying elongation and waist cross section using conservation of glass volume, as follows. A stretched fiber will adopt some tapered shape as shown in Fig. 1. For any taper curve, the volume of glass in the tapered region is given by

$$V = S_0 \int_{-L/2}^{L/2} \left(\frac{r(\ell)}{R_0}\right)^2 \mathrm{d}\ell = S_0 L\, f\left(\sqrt{\frac{S}{S_0}}\right) = S_0 L\, f\,(\mathrm{ITR}), \tag{4}$$

where S_0 is the original cross section, $r(\ell)$ represents the taper shape (see Fig. 1), and $f(\mathrm{ITR})$ is the integrated taper function. The parameter

$$\mathrm{ITR} = \sqrt{\frac{S}{S_0}}, \tag{5}$$

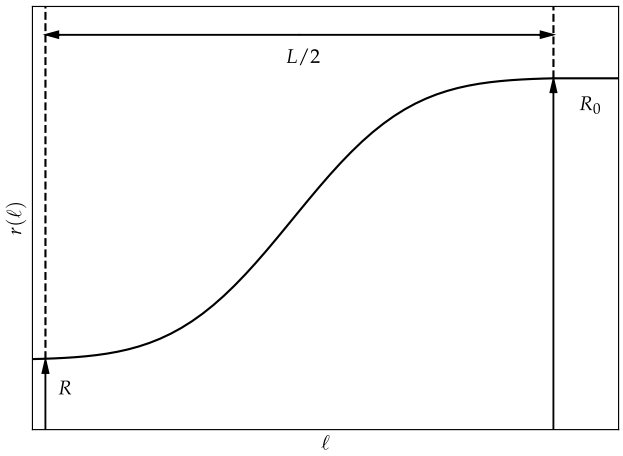

Fig. 1. Right and top half of the cross section of an optical fiber taper showing initial radius R_0 and waist radius R. The curve $r(\ell)$ shown is arbitrary. The full taper length is L.

which appears naturally in Eq. (5), is the inverse taper ratio (ITR). It is a key parameter for taper and fused coupler fabrication. For cylindrical fibers, it reduces to R/R_0.

Inverting f and applying the volume conservation condition $V = V_0 = L_0 S_0$, we find

$$S = S_0\left[f^{-1}\left(\frac{L_0}{L}\right)\right]^2, \tag{6}$$

which can be injected into Eq. (3) to yield

$$\left[f^{-1}\left(\frac{L_0}{L}\right)\right]^2 \frac{\mathrm{d}L}{L_0} = \frac{F}{\eta_e S_0}\mathrm{d}t. \tag{7}$$

Integrating on both sides, we get

$$\mathcal{F}(L/L_0) = \frac{Ft}{\eta_e S_0}, \tag{8}$$

with

$$\mathcal{F}(L/L_0) \equiv \int_1^{\xi} \left[f^{-1}(1/\xi)\right]^2 \mathrm{d}\xi, \tag{9}$$

using the change of variable $\xi = L/L_0$.

Finally, we find that the strain equation for an arbitrary taper curve as a function of the viscosity of the glass is

$$\epsilon = \mathcal{F}^{-1}\left[\frac{Ft}{\eta_e S_0}\right] - 1. \tag{10}$$

B. Taper Shape

To apply Eq. (10), we need to assume a shape $r(l)$ for the taper. The simplest continuous case is that of a linear shape, as shown in Fig. 2. The slope equation is then

$$r(\ell) = R + 2(R_0 - R)\frac{\ell}{L}, \tag{11}$$

leading to

$$\frac{Ft}{\eta_e S_0} = \int_1^{L/L_0} \mathrm{d}\xi \left[\frac{-1}{2} + \frac{3}{\xi} + \frac{\sqrt{3}}{2}\sqrt{\frac{4}{\xi} - 1}\right]. \tag{12}$$

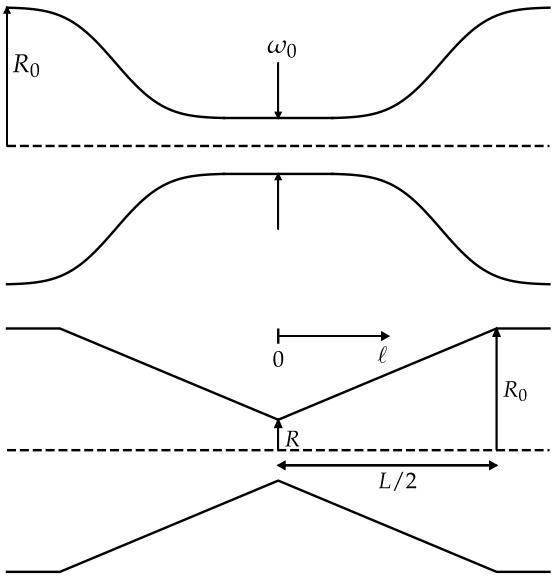

Fig. 2. Top: fiber taper shape. Initial fiber radius is R_0. The waist ω_0 corresponds to the taper's smallest diameter. Bottom: taper shape assumption with linear slopes.

The integral can be analytically resolved, but the result has to be inverted numerically.

3. EXPERIMENTAL SETUP

In this section, we first describe the experimental setup to measure the strain curves from a fiber under a stress. Using Eq. (10) and the model described by Eqs. (11) and (12), we are able to find the viscosity. We second describe the setup used for fiber taper fabrication.

A. Viscosity Measurements

Figure 3 presents the experimental setup used to measure viscosity. Two blocks (yellow) with V-grooves supported an optical fiber with a load of mass m attached to its end. The applied load hung from the optical fiber on a frictionless 7.62 cm (3-inch) diameter pulley. The fiber's stripped section set between the two blocks was heated at a fixed process temperature by a flow of heated air. A thermocouple displaced along the airflow 0.1 mm at a time measured the process temperature profile. The heated section L_0 corresponds to the length perpendicular to the airflow within 2°C of the maximum process temperature, which corresponds to twice the accuracy of the process temperature measurement.

1. Material

We measured the viscosity of two different fibers made of fluoride glass. Table 1 presents the specifications of the two MM fibers described in this paper: a ZBLAN fiber (210603/TB 123, Le Verre Fluoré, France) and a fluoroindate fiber (IRFH10026, Thorlabs, USA).

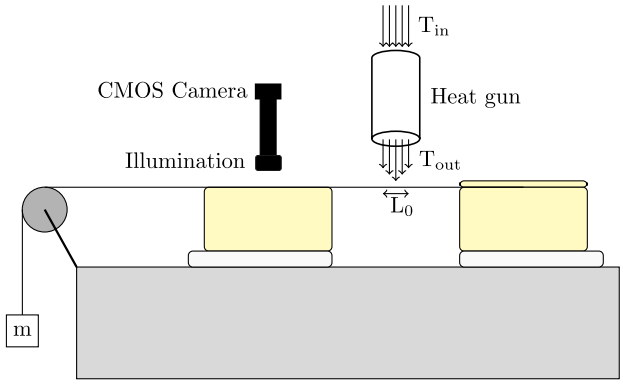

Fig. 3. Experimental setup for viscosity measurements. The optical fiber is kept in place by the clamp on the right block but free from attachment on the left block. The fiber is stripped of its coating over the heated section L_0.

Table 1. Fluoride Fiber Specifications [a]

Fibers	ZBLAN	Fluoroindate
Diameter core/clad/coating [μm]	90/150/220	100/192/287
Cladding diameter tolerance [μm]	±5	±2.5
Glass-transition temperature (T_g) [°C]	≈259 [32]	≈300 [31]
Crystallization temperature (T_x) [°C]	≈359 [32]	≈400 [33]
Supplier	Le Verre Fluoré	Thorlabs

[a] T_g and T_x depend on the glass composition and may vary.

2. Data Acquisition

We acquired fiber displacement data using a CMOS camera (DCC1545M-GL) over the left block. The reference point used was a white piece of tape used as a marker fixed on the optical fiber. The white marker displacement was filmed at an acquisition rate of 10 frames per second (FPS) while the fiber was heated. A homemade type-K thermocouple that fits on the blocks was used to measure the process temperature at the fiber position of the fiber after each test. The uncertainty on the process temperature was ±1°C and was limited by the accuracy of the thermometer. Moreover, the measured process temperatures were subject to a bias error not quantified yet. Therefore, measured process temperatures should be considered relative values rather than absolute reference points. Room temperature and humidity were recorded at the start of each day of experiments with a hygrothermometer (Testo 623).

B. Data Analysis

An edge-detection algorithm was used in post-processing to detect the marker's position and reconstruct the fiber's displacement over time. The algorithm first subtracted the first frame of the video from all other frames to suppress background and remove static components. A Sobel filter applied to selected pixel lines showing the marker led to the image gradient. The

gradient obtained from the Sobel filter was squared, then averaged over 10 lines to highlight the marker's edges. The marker's position was saved by indexing the position of its edge. Time was calculated as the number of frames divided by the acquisition frequency. The position was converted from pixel units to distance units (mm) using a calibration factor obtained by imaging a ruler. Appendix A presents the uncertainty analysis and fit accuracy. The position uncertainty established was of two pixels. The data extracted from the algorithm gave the fiber's displacement $(L(t) - L_0)$. Equation (13) was used to find the strain from it:

$$\epsilon = \frac{c(L(t) - L_0)}{L_0}, \tag{13}$$

where c is the calibration factor used to convert data from pixel to mm. The calibration factor was determined over a sample containing 47 pictures of a ruler all taken at the same parameters. The calibration factor's value was the sample mean, and the uncertainty was its standard deviation. Python Scipy's library was used to fit the theoretical model on the displacement data. Both the data points and their uncertainty were the input of the *curve_fit* function. From Eq. (10), the algorithm found a value for $\alpha = F/\eta_e S_0$. The uncertainty over the viscosity was again found using the partial derivative method (Appendix A). The uncertainty associated with the time conversion from the frequency is negligible, as specified by the manufacturer.

C. Fiber Tapers

The setup for taper fabrication used the same blocks and heat source for the viscosity tests, albeit with the fiber clamped on both blocks. As shown in Fig. 4, the heat source swept the optical fiber on a length $\Delta = 6$ mm, while slowly stepping away from the fiber. The two blocks stretched the fiber at a velocity of $v_0 = 0.2$ mm/s. The fiber taper's optical properties were measured during the tapering process. A broadband light source (HP 83437a) with a SM output was coupled to the fluoroindate fiber by a mechanical junction. An integrating sphere power sensor detected the signal and sent it to a computer. Thorlab's PM100USB and its associated software (Optical Power Monitor) were used to read the transmission values. Data were acquired and recorded with an averaging over 100 points. The same CMOS camera and illumination system from Fig. 3 acquired the taper pictures. The camera could be moved over the left and right blocks when the heat source was away from the taper.

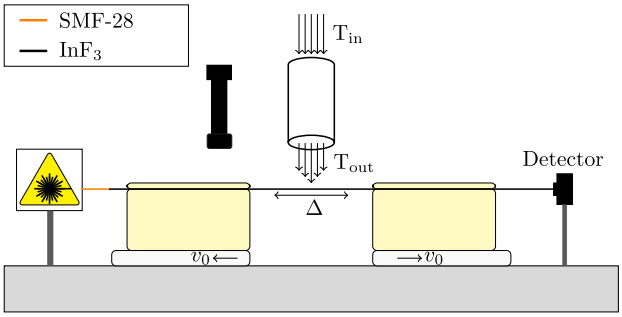

Fig. 4. Experimental setup for taper fabrication and transmission loss measurements. A heat source heats the fiber at a selected process temperature on a length of Δ. The blocks stretch the fiber at velocity v_0. The transmission loss is simultaneously measured by a broadband source coupled to the fluoride fiber and an integrating sphere power sensor. The taper images are acquired with a camera.

4. VISCOSITY RESULTS

Figure 5 presents typical displacement curves and their respective fits for a fluoroindate optical fiber. Displacement curves are acquired with a heated length L_0 of 0.5 ± 0.1 mm and an applied load of 14.16 ± 0.01 g. The vertical axis corresponds to the displacement in mm. Each point represents the extracted position by the algorithm. The blue line corresponds to the accuracy of each data point. It is mainly not perceptible. Viscosity values are extracted from Eq. (10)'s fit parameters in units of Pa's. Since all viscosities are presented in a base-10 logarithm, the viscosity will be presented in $\log_{10}(\text{Pa} \cdot \text{s})$. Two sets of experiments were conducted: variation of applied load at constant process temperature and variation of process temperature at constant load. In Fig. 5, the displacement curves are acquired at process temperatures of 248°, 252°, 254°, 257°, and 261°C. A higher heating process temperature causes the fiber's viscosity to decrease. The resulting displacement is, therefore, faster for higher process temperatures. The viscosity results extracted from displacement curves in Fig. 5 are in Table 2 with results from ZBLAN as well.

The results for load variation at constant process temperature are presented in Table 3. Viscosity results do not reveal any significant dependency between applied load and viscosity. A higher applied load yields faster displacements from Eq. (10), but the derived viscosity is expected to remain unaffected. The applied loads are chosen to provide equivalent initial stress on both fibers.

Figures 6 and 7 present the decreasing viscosity with process temperature for ZBLAN and fluoroindate optical fibers. The viscosity values are fitted linearly (in semi-logarithmic scale) to follow the viscosity variation with process temperature over a small range. The linear fit gives reliable results with a R-squared coefficient >0.95 for both fibers. The slope from the fit shows how the viscosity varies with process temperature: viscosity doubles every 1.3°C in the range between 241°C and 251°C for ZBLAN. In a similar process temperature range, from 248°C to 261°C, fluoroindate's viscosity doubles every 1.5°C. The accuracy of the linear fit comes from the co-variance values given by the fit's parameters. Viscosity tests were also conducted on SMF-28 silica fiber, which acts as the gold standard for fused component fabrication. For silica fiber, typical components are made at viscosities between 7 and 9 $\log_{10}(\text{Pa} \cdot \text{s})$.

A. Crystallization

Two tests were conducted on fluoroindate fibers to investigate crystallization effects. Two viscosity tests were stopped at different displacements: 0.15 and 0.6 mm. Figure 8 shows the tapers resulting from the experiments. Surface crystallization appears only on the taper made from a displacement of 0.61 ± 0.01 mm. Crystallization is apparent by the fiber's grainy aspect at its surface.

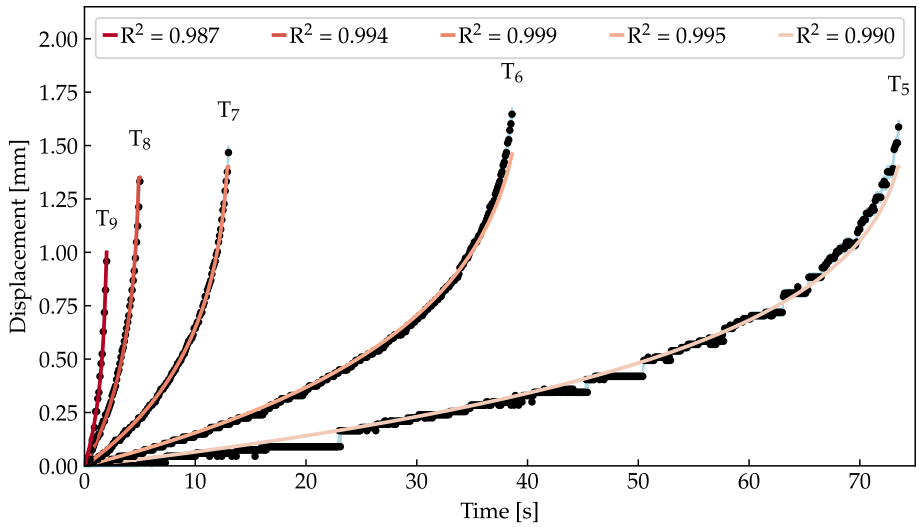

Fig. 5. Displacement of fluoroindate optical fiber under different process temperatures at fixed load of 14.16 g. Blue area represents precision over each data point. Process temperatures from T_5 to T_9 are 248°, 252°, 254°, 257°, and 261°C, respectively, with accuracy of ±1°C.

Table 2. Viscosity (base-10 logarithm) and R-squared Coefficients for the Displacement Curves from Fig. 5 [a]

	Process Temperature [°C]	$\log_{10}$ (viscosity) [$\log_{10}$ (Pa · s)]	R-squared [-]
ZBLAN			
T_1	241	8.83 ± 0.06	0.995
T_2	244	8.39 ± 0.06	0.990
T_3	247	7.57 ± 0.06	0.997
T_4	251	7.11 ± 0.06	0.952
Fluoroindate			
T_5	248	8.87 ± 0.02	0.990
T_6	252	8.59 ± 0.02	0.997
T_7	254	8.11 ± 0.02	0.999
T_8	257	7.70 ± 0.02	0.997
T_9	261	7.30 ± 0.02	0.988

[a] Applied loads are, respectively, 11.08 ± 0.01 g and 14.13 ± 0.01 g for ZBLAN and fluoroindate fibers. Accuracy of process temperature is ±1°C.

Table 3. Viscosity (base-10 logarithm) and R-squared Coefficients for Different Loads [a]

	Load [g]	$\log_{10}$ (viscosity) [$\log_{10}$ (Pa · s)]	R-squared [-]
ZBLAN			
m_1	11.08	8.83 ± 0.06	0.995
m_2	18.12	8.59 ± 0.06	0.996
m_3	21.24	8.66 ± 0.06	0.997
m_4	33.33	8.57 ± 0.06	0.994
Indium Fluoride			
m_5	14.13	8.87 ± 0.02	0.990
m_6	22.21	9.01 ± 0.02	0.999
m_7	26.22	8.95 ± 0.02	0.999
m_8	44.67	8.79 ± 0.03	0.989

[a] The process temperatures are kept constant at 241 ± 1°C and 248 ± 1°C for ZBLAN and fluoroindate, respectively. Load accuracy is of ±0.01 g.

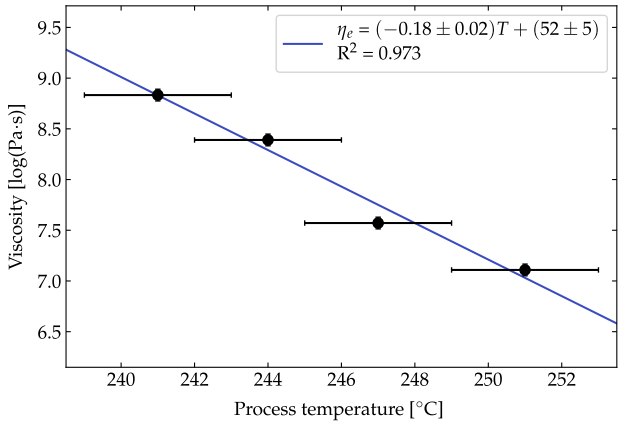

Fig. 6. Viscosity (base-10 logarithm) as a function of process temperature for ZBLAN optical fibers. Glass transition temperature for ZBLAN is 259°C, outside the measurement range. Applied load is 11.08 ± 0.01 g. High uncertainty on the process temperature is due to the limited accuracy of the thermometer [±1°C]. Room temperature: 23.6°C, humidity: 64.7%.

Table 4. Viscosity (base-10 logarithm) and R-squared Coefficients for Two Viscosity Tests on Fluoroindate Fibers Stopped at Different Displacement Values [a]

	Displacement [mm]	$\log_{10}$ (viscosity) [$\log_{10}$ (Pa · s)]	R-squared [-]
Indium Fluoride			
c_1	0.150 ± 0.008	8.9 ± 0.3	0.988
c_2	0.61 ± 0.01	9.1 ± 0.1	0.995

[a] Applied load is 14.13 ± 0.01g for both tests. Room temperature: 24°C, humidity: 34.8%.

Table 4 presents viscosity values found for each test. We also observed that both tapers fabricated with the same initial conditions exhibit the same viscosity within measurement accuracy.

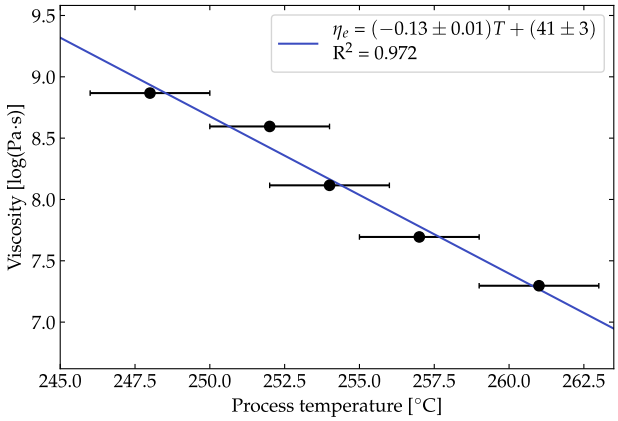

Fig. 7. Viscosity (base-10 logarithm) as a function of process temperature for fluoroindate optical fibers. Glass transition temperature for fluoroindate glass is 300°C, outside the measurement range. Applied load is 14.13 ± 0.01 g . Room temperature: 23.7°C, humidity: 54.6%.

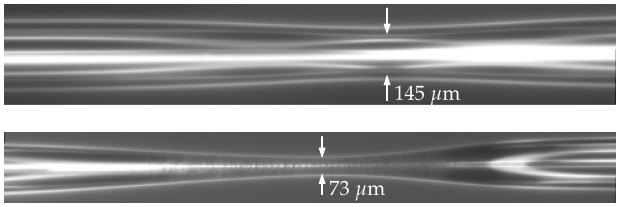

Fig. 8. Tapers made from a viscosity test on a fluoroindate fiber at a process temperature of 250 ± 1°C with a load of 11.08 ± 0.01 g . Top: test is stopped when the fiber reaches a displacement of 0.15 ± 0.03 mm . No crystallization is apparent. Bottom: the test is stopped when the fiber reaches a displacement of 0.61 ± 0.07 mm . Surface crystallization is apparent. Room temperature: 24°C, humidity: 34.8%.

5. FLUOROINDATE FIBER TAPERS

Using results from the viscosity measurements, fluoroindate fibers were tapered to various ITRs, as defined before. Initially, three tapers of ITR 0.2 were made using selected viscosity values from Fig. 7. The taper recipe consists of heating the fiber over a fixed length ($\Delta = 6$ mm) while stretching at a constant velocity ($v = 200$ μm/s) until the desired ITR, as assessed by the camera. Transmission values for these three tapers are presented in Table 5. Tapers 2 and 3 suffer from additional losses, which are presumed to come from material degradation. Figure 9 shows the three tapers waists, with increasing crystallization for smaller viscosity values. ITR values were calculated using taper shape equations [23] and validated with the camera. All ITR values were measured with an absolute accuracy better than ± 0.03 .

The transmission losses at ITR 0.2 (Table 5) are consistent with the degradation of the fiber observed in Fig. 9. The presence of granularity, precisely in middle and bottom tapers, is an indication of crystallization. Fiber tapers made at higher viscosity values tend to preserve chemical and optical properties better.

Taper recipes were optimized to reach ITR 0.12 at an initial viscosity of 8.75 ± 0.05 log(Pa · s) . A total of seven tapers were tested. Losses on three tapers were lower than <0.1 dB , down to ITR 0.3. The other four tapers exhibited losses around 0.15 dB at ITR 0.3. The best tapers were produced over a span of two days. In general, intraday repeatability was very high, but reproducibility over several weeks was challenging. Figure 10 shows typical taper loss as a function of ITR for a fluoroindate fiber with initial viscosity of 8.75 ± 0.05 $\log_{10}$ (Pa · s). Losses remain low up to ITR 0.3. A significant increase in loss occurs for lower ITRs. At ITR 0.3, measured power offers losses of -0.042 dB , while it decreases to -0.349 dB at ITR 0.2, and to -3.263 dB at ITR 0.12. The shaded area corresponds to ITRs at which simple fused couplers are typically fabricated. Accuracy over loss is ± 0.002 dB . Losses during tapering occur from higher-order modes not being supported by a smaller-diameter fiber and leaking outside of the cladding. Experimentally measured taper losses were compared to two propagation models in tapers. Both models take into account the excitation of all bound and tunnel modes [34] at the input of the fiber. The second model further assumes that all tunnel modes leak outside of the fiber at the tapering transitions. Experimental data closely follow the second model, which suggests excess losses of 0.4 dB at an ITR of 0.12 for the lowest-order modes.

Figure 11 shows the taper appearance at various ITRs. Taper slope (top) and taper waist at ITR 0.2 (middle) remain free of defects or crystallization. The taper picture at ITR 0.12 (bottom) is grainier, which indicates crystallization.

Table 5. Transmission Loss for Three Fluoroindate Tapers of ITR 0.2 and Their Respective Viscosities[a]

	$\log_{10}$ (viscosity) [$\log_{10}$ (Pa · s)]	Transmission Loss [dB]
Taper 1	8.79	−0.266
Taper 2	7.96	−0.682
Taper 3	7.54	−2.581

[a] Accuracy on viscosity is ± 0.02 $\log_{10}$ (Pa · s) and ± 0.002 dB on transmission loss. Room temperature: 22.8°C, humidity: 18.3%.

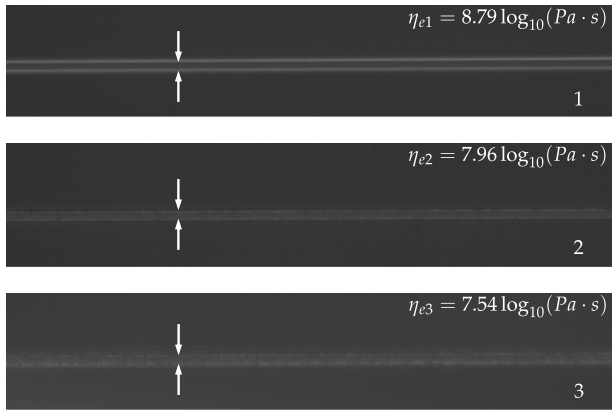

Fig. 9. From top to bottom, waists of tapers 1–3 described in Table 5 for an ITR of 0.2, and their initial viscosity values expressed in $\log_{10}$ (Pa · s). The crystallization signature—grainy appearance—increases as viscosity decreases. Room temperature: 22.8°C, humidity: 18.3%.

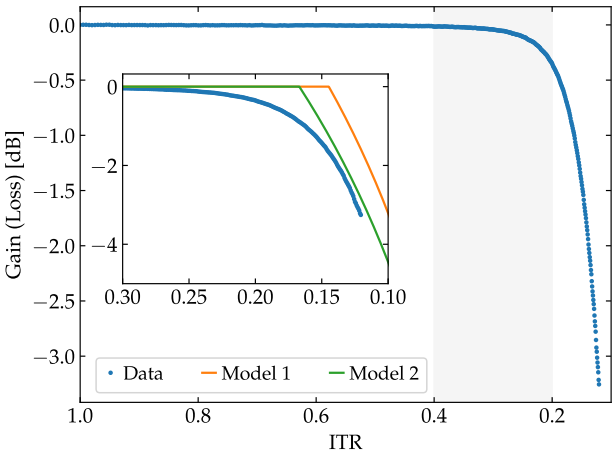

Fig. 10. Loss as a function of ITR for a fluoroindate taper heated over a constant 6 mm length, and made with an initial viscosity of $8.75 \pm 0.05 \log_{10}(\text{Pa} \cdot \text{s})$. The shaded area shows the ITR regime useful for coupler fabrication. Losses are negligible up to ITR 0.3. Inset graph zooms in on ITRs ranging from 0.3 to 0.1 comparing experimental data (blue points) with two models of modal losses (model 1 in orange, model 2 in green). Room temperature: 22.8°C, humidity: 18.3%.

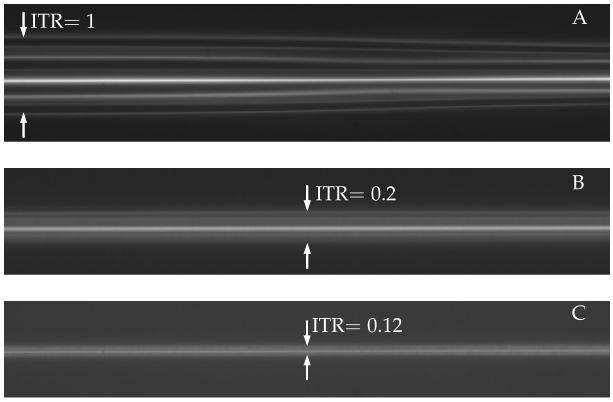

Fig. 11. Waist of two tapers (B and C) made with the same recipe and initial viscosity. Taper B was stopped at ITR 0.2, and taper C at ITR 0.12. The top picture (A) represents the left slope. Crystallization is visible only at ITR 0.12. The fiber has an initial diameter of 192 μm. Room temperature: 24°C, humidity: 34.8%.

6. DISCUSSION

Viscosity is a property of paramount importance for the fusing and tapering of optical fibers, especially in the context of fluoride glasses.

Our model developed in Section 2 reliably predicts displacement results presented in Fig. 5 and in Tables 2 and 3 with viscosity as the single free parameter. The model quantitatively matches experimental data and enables to obtain viscosity with low uncertainty, as measured by the R-squared coefficients of the fits. We observed slightly lower R-squared coefficients at the highest process temperatures and highest loads, which correspond to experimental situations where displacements are much faster and the number of measured points is limited by the acquisition frequency of the camera. Overall, the model and experimental method are well validated by the results.

Our results are highly repeatable: uncertainty on repeatedly measured values is very low when environmental conditions are well replicated. However, working with fluoride glasses is challenging. The glasses themselves suffer variations in chemical composition and physical parameters from one batch to another. In addition, their physical behavior is very sensitive to environmental variations, particularly room temperature and humidity levels. Consequently, results were not easily reproducible on a week-to-week basis. This accounts for some of the variations observed in our results when experimental parameters were varied.

Additional sources of uncertainty due to difficult-to-reproduce conditions include the temperature and flow rate of the source of heated flow. For instance, multiple tests conducted over an extended period would yield slightly increasing viscosity values due to the tendency of the heat source to warm up over time.

More physical parameters, such as increasing crystallization at higher process temperatures [35], also increase uncertainty, although results from Table 4 indicate that this effect was minimal throughout our experiments. Even when crystallization is limited to the cladding, it affects taper losses in MM fibers, as higher-order modes are not guided in the core. The full impact of crystallization on the physical properties of fluoride fibers is yet to be determined.

Overall, the accuracy of our measurements suffers more from environmental factors than anything else. To make full use of viscosity measurements in the manufacturing of fiber components, best practices would include frequent measurements of viscosity versus process temperature, to ensure the best possible tailoring of fabrication parameters.

We expect heated glass to behave as a Newtonian fluid so that our measurements should not depend on the applied stress. Table 3 seems to confirm the hypothesis except for the viscosity value associated with m_1 (smallest load), which is relatively higher than all other measured viscosities of ZBLAN. Several factors can explain this apparent discrepancy, including friction, which is negligible for larger loads but can reduce the velocity for lower loads. This in turn results in higher apparent viscosity. However, other explanations are as plausible, including a lack of reproducibility as seen above.

In the literature, multiple models are used to describe viscosity variance with temperature. The Fulcher or the Arrhenius equations are typically used for oxide glass melts. However, the viscosity variance of fluoride glasses cannot be expressed by them [36]. Models used to fit viscosity are usually empirical and depend largely on the composition of the fibers' glass. As a result, we chose a linear model to describe the relation of the logarithm of viscosity with respect to process temperature over a limited range.

The resulting Figs. 6 and 7 are key results for taper fabrication. Absolute values of the process temperature ranges should not be taken as references, as they are likely subject to bias errors. But it is the slopes of the curves that contain the most important information. For both fibers, the decrease in viscosity observed between solid ($\sim 10^9$ Pa · s) and fluid ($\sim 10^7$ Pa · s) glass states occurs over a small range of close to 10°C. In comparison, the same decrease occurs over a process temperature range of more than 200°C [37] for silica fibers. Hence, process temperature

control to within a few degrees seems required to fabricate tapers and couplers using fluoride glasses. This probably constitutes one of the biggest hurdles for the technology. But with a good viscosity characterization setup, the process should be much easier to handle.

Our viscosity measurements show that fluoroindate fibers have higher process temperatures and slightly wider ranges of useful process temperatures for component fabrication than ZBLAN fibers.

In our fabrication tests (Table 5 and Fig. 9), we observed both mechanical and optical degradation at lower viscosities, mainly due to faster crystallization rates.

The best taper results were obtained in high-viscosity conditions, with virtually no crystallization at targeted ITR for coupler fabrication, as shown in Fig. 11.

Fused components are fabricated by fusing two fibers and stretching them to ITRs between 0.4 and 0.2. Figure 10 shows losses starting at around 0.3 ITR. Our best model indicates that excess losses as low as 0.4 dB are possible at 0.12 ITR. These observations support the feasibility of fused MM fluoroindate couplers in the near future.

7. CONCLUSION

Fluoride glass fibers show a lot of promise for all-fiber fused components in the mid-IR. However, their challenging mechanical properties have so far slowed down the development of these components. Among important considerations, the rapid variation of the viscosity of fluoride glasses with temperature plays a significant role in the manufacturing of fused components and needs to be studied carefully. We have presented a simple and reliable experimental setup and theoretical model to measure the viscosity of a fiber. Our method, applied to two different kinds of fluoride optical fibers, ZBLAN and fluoroindate, shows a significant viscosity decrease over process temperature in a range close to 10°C for both fibers. The window for operation thus appears very narrow, but our setup, which relies on the same components as those used for fabrication, leads to a simple way of choosing the right operating temperature. Our results also show that fluoroindate fibers might be the better candidates for optical fiber components, as their viscosity decrease is in a broader range. We used our viscosity characterization method to find the correct operating parameters to fabricate low-loss tapers, down to an ITR of 0.3, without visible defects or crystallization. Our method thus opens the doors to robust manufacturing methods for high-performance fused components for the mid-IR.

APPENDIX A: UNCERTAINTY OF MEASUREMENT

We followed the procedures outlined in the "Guide to the expression of uncertainty in measurement" (GUM) [38] for all uncertainty analyses. To the extent that it was possible, we used statistical means to compute an estimated mean value $\langle X\rangle$ and estimated variance S_X^2 of a variable X. The value and uncertainty associated with that variable were then taken as the estimated mean and estimated standard deviation S_X, respectively. Some uncertainties (e.g., the real-life length associated with the pixel width of our camera) had to be estimated by other means (e.g., by counting the pixels between two notches on a ruler). To propagate uncertainties, for a function $f(X_1, \cdots, X_n)$ of n variables, we first estimate all the components S_{X_i,X_j} of the covariance matrix Σ_X, with

$$S_{X_i,X_j} = \big\langle (X_i - \langle X_i\rangle)(X_j - \langle X_j\rangle)\big\rangle = \langle X_i X_j\rangle - \langle X_i\rangle\langle X_j\rangle. \tag{A1}$$

In particular, $S_{X_i,X_i} = S_{X_i}^2$.

We then compute the Jacobian

$$J_f = [J_1, \cdots, J_n], \tag{A2}$$

where

$$J_i = \left.\frac{\partial f}{\partial X_i}\right|_{\langle X_1\rangle,\cdots,\langle X_n\rangle}. \tag{A3}$$

The estimated uncertainty S_f for the value of the function f is then given by

$$S_f^2 = J_f \Sigma_X J_f^T, \tag{A4}$$

where $\bullet^T$ denotes transposition.

For n independent variables, the formula simplifies to

$$S_f^2 = \sum_{i=1}^{n} \left(S_{X_i} J_i\right)^2. \tag{A5}$$

Funding. Natural Sciences and Engineering Research Council of Canada (5006404, 5011666); Fonds de Recherche du Québec - Nature et Technologies (208631).

Acknowledgment. The authors thank Mikaël Leduc from Laboratoire des Fibres Optiques (LFO) for support and guidance, and Xavier Attendu, Simon Brais-Brunet, Raphael Maltais-Tariant, and Martin Poinsinet-de Sivry Houle for useful discussions. The authors also acknowledge Le Verre Fluoré and Thorlabs for kindly supplying, respectively, ZBLAN and fluoroindate optical fibers. This research was undertaken thanks in part to funding from the Canada First Research Excellence Fund through the TransMedTech Institute.

Disclosures. Caroline Boudoux and Nicolas Godbout are founding partners of Castor Optics, Inc.

Data availability. Data underlying the results presented in this paper are not publicly available at this time but may be obtained from the authors upon reasonable request.

REFERENCES

1. A. K. Agarwal, "Review of optical fiber couplers," Fiber Integr. Opt. **6**, 27–53 (1987).
2. D. Nolan, "Tapered-fiber couplers, MUX and DEMUX," in *Handbook of Optics* (McGraw Hill 2000), Vol. **4**.
3. N. Godbout, C. Boudoux, W.-J. Madore, S. Lemire-renaud, X. Daxhelet, and M. Leduc, "Asymmetric optical fiber coupler," U.S. patent9,753,222 (September 5, 2017).
4. M. P. de Sivry-Houle, S. B. Beaudoin, S. Brais-Brunet, M. Dehaes, N. Godbout, and C. Boudoux, "All-fiber few-mode optical coherence tomography using a modally-specific photonic lantern," Biomed. Opt. Express **12**, 5704–5719 (2021).
5. H. Bao, S. Y. Ryu, B. H. Lee, W. Tao, and M. Gu, "Nonlinear endomicroscopy using a double-clad fiber coupler," Opt. Lett. **35**, 995–997 (2010).
6. W.-J. Madore, E. De Montigny, O. Ouellette, S. Lemire-Renaud, M. Leduc, X. Daxhelet, N. Godbout, and C. Boudoux, "Asymmetric double-clad fiber couplers for endoscopy," Opt. Lett. **38**, 4514–4517 (2013).

7. D. Lorenser, B. C. Quirk, M. Auger, W.-J. Madore, R. W. Kirk, N. Godbout, D. D. Sampson, C. Boudoux, and R. A. McLaughlin, "Dual-modality needle probe for combined fluorescence imaging and three-dimensional optical coherence tomography," Opt. Lett. **38**, 266–268 (2013).
8. J. Mavadia, J. Xi, Y. Chen, and X. Li, "An all-fiber-optic endoscopy platform for simultaneous oct and fluorescence imaging," Biomed. Opt. Express **3**, 2851–2859 (2012).
9. K. Beaudette, H. W. Baac, W.-J. Madore, M. Villiger, N. Godbout, B. E. Bouma, and C. Boudoux, "Laser tissue coagulation and concurrent optical coherence tomography through a double-clad fiber coupler," Biomed. Opt. Express **6**, 1293–1303 (2015).
10. R. Maltais-Tariant, C. Boudoux, and N. Uribe-Patarroyo, "Real-time co-localized oct surveillance of laser therapy using motion corrected speckle decorrelation," Biomed. Opt. Express **11**, 2925–2950 (2020).
11. A. Schliesser, N. Picqué, and T. W. Hänsch, "Mid-infrared frequency combs," Nat. Photonics **6**, 440–449 (2012).
12. M. Kumar, M. N. Islam, F. L. Terry, M. J. Freeman, A. Chan, M. Neelakandan, and T. Manzur, "Stand-off detection of solid targets with diffuse reflection spectroscopy using a high-power mid-infrared supercontinuum source," Appl. Opt. **51**, 2794–2807 (2012).
13. C. Wang and P. Sahay, "Breath analysis using laser spectroscopic techniques: breath biomarkers, spectral fingerprints, and detection limits," Sensors **9**, 8230–8262 (2009).
14. L. Ha, M. Jaspan, D. Welford, M. Evers, G. Kositratna, M. J. Casper, D. Manstein, and R. Birngruber, "First assessment of a carbon monoxide laser and a thulium fiber laser for fractional ablation of skin," Lasers Surg. Med. **52**, 788–798 (2020).
15. M. Bernier, D. Faucher, N. Caron, and R. Vallée, "Highly stable and efficient erbium-doped 2.8 μm all fiber laser," Opt. Express **17**, 16941–16946 (2009).
16. S. Duval, M. Bernier, V. Fortin, J. Genest, M. Piché, and R. Vallée, "Femtosecond fiber lasers reach the mid-infrared," Optica **2**, 623–626 (2015).
17. T. Yamamoto, T. Komukai, and Y. Miyajima, "Wide band erbium-doped fluoride fiber optical amplifier at 2.7 μm with fluoride fiber wavelength-division multiplex coupler," Jpn. J. Appl. Phys. **32**, L62 (1993).
18. S. T. Nicholls and M. Scott, "Method of making fluoride glass optical coupler," U.S. patent5,139,550 (18 August1992).
19. G. Stevens and T. Woodbridge, "Mid-IR fused fiber couplers," Proc. SPIE **9730**, 973007 (2016).
20. Y. Wang, G. Zhu, M. Li, R. Singh, C. Marques, R. Min, B. K. Kaushik, B. Zhang, R. Jha, and S. Kumar, "Water pollutants p-cresol detection based on Au-ZnO nanoparticles modified tapered optical fiber," IEEE Trans. Nanobiosci. **20**, 377–384 (2021).
21. Z. Wang, R. Singh, C. Marques, R. Jha, B. Zhang, and S. Kumar, "Taper-in-taper fiber structure-based LSPR sensor for alanine aminotransferase detection," Opt. Express **29**, 43793–43810 (2021).
22. L.-Y. Shao, J. Canning, T. Wang, K. Cook, and H.-Y. Tam, "Viscosity of silica optical fibres characterized using regenerated gratings," Acta Mater. **61**, 6071–6081 (2013).
23. T. A. Birks and Y. W. Li, "The shape of fiber tapers," J. Lightwave Technol. **10**, 432–438 (1992).
24. S. Lacroix, N. Godbout, and X. Daxhelet, "Optical fiber components: design and applications of fused biconical tapered components," in *Optical Fiber Components: Design and Applications* (Research Signpost, 2006).
25. M. Saad, "Fluoride glass fiber: state of the art," Proc. SPIE **7316**, 73160N (2009).
26. K. Matusita, M. Koide, and T. Komatsu, "Viscous flow mechanism of fluoride glasses over a wide temperature range," J. Non-Cryst. Solids **140**, 141–145 (1992).
27. M. Poulain and G. Mazé, "Chemistry of fluoride glasses [–a review]," Chemtronics **3**, 77–85 (1988).
28. C. Day, P. France, S. Carter, M. Moore, and J. Williams, "Fluoride fibres for optical transmission," Opt. Quantum Electron. **22**, 259–277 (1990).
29. R. R. Gattass, R. Thapa, F. H. Kung, L. E. Busse, L. B. Shaw, and J. S. Sanghera, "Review of infrared fiber-based components," Appl. Opt. **54**, F25–F34 (2015).
30. M. Gorjan, R. Petkovšek, M. Marinček, and M. Čopič, "High-power pulsed diode-pumped Er: ZBLAN fiber laser," Opt. Lett. **36**, 1923–1925 (2011).
31. M. Saad, "Indium fluoride glass fibers," Proc. SPIE **8275**, 82750D (2012).
32. J. A. Harrington, *Infrared Fibers and their Applications* (SPIE, 2004).
33. P. P. Fedorov, R. M. Zakalyukin, L. N. Ignat'eva, and V. M. Bouznik, "Fluoroindate glasses," Russ. Chem. Rev. **69**, 705–716 (2000).
34. A. W. Snyder and J. D. Love, "Fundamental properties of modes," in *Optical Waveguide Theory* (Springer, 1983), pp. 208–237.
35. D. Homa, G. Pickrell, and A. Wang, "Investigation of high temperature silica based fiber optic materials," Tech. Rep. (Virginia Polytechnic Institute, 2018).
36. G. Zhang, J. Jiang, M. Poulain, A. Delben, and J. Delben, "Viscosity of fluoride glasses near the fiber drawing temperature region," J. Non-Cryst. Solids **256**, 135–142 (1999).
37. G. Urbain, Y. Bottinga, and P. Richet, "Viscosity of liquid silica, silicates and alumino-silicates," Geochim. Cosmochim. Acta **46**, 1061–1072 (1982).
38. Joint Committee for Guides in Metrology, BIPM Paris, "Evaluation of measurement data — Guide to the expression of uncertainty in measurement," JCGM 100:2008 (2008).